Materials Horizons

ROYAL SOCIETY OF CHEMISTRY

COMMUNICATION

View Article Online
View Journal | View Issue

Cite this: *Mater. Horiz.*, 2026, **13**, 2583

Received 30th September 2025,
Accepted 11th December 2025

DOI: 10.1039/d5mh01871d

rsc.li/materials-horizons

Ambipolar to anti-ambipolar light-induced transition in WSe_2-based FETs

Kimberly Intonti,*[ab] Adolfo Mazzotti,[a] Aniello Pelella,[a] Filippo Giubileo,[b] Nadia Martucciello,[b] Stephen O'Sullivan,[c] Vilas Patil,[c] Paul K. Hurley,[cd] Lida Ansari,[c] Farzan Gity[c] and Antonio Di Bartolomeo*[a]

The growing need for efficient processing of large amounts of data in compact electronic systems is driving interest in investigating alternative device architectures. 2D material-based devices exhibiting anti-ambipolar behaviour represent a promising option to address this need. In this work, we investigate a WSe_2-based field-effect transistor that shows ambipolar conduction with dominant n-type behaviour in the dark. Under illumination, using either diffuse white LED light or a collimated red laser, the device exhibits a transition to anti-ambipolar transport, with a prominent current peak in a narrow driving voltage range, which is desirable for fast switching logic applications. This response allows for the identification, under controlled illumination conditions, of three distinct current levels in three different bias regions, which are suitable for implementing a three-state logic device. The peak amplitude varies linearly with light intensity, and the corresponding photodetection performance results in a significant responsivity of 0.13 A W^{-1} under red laser illumination. The light-induced transition from ambipolar to anti-ambipolar behaviour is qualitatively described through energy band diagrams, with the photocurrent peak corresponding to the n–p transition point observed in the dark.

New concepts

We report a new mechanism to achieve anti-ambipolar transport in a WSe_2-based field-effect transistor (FET) through a light-tunable transition from its intrinsic ambipolar behavior. While anti-ambipolar responses in 2D devices have so far been primarily realized in carefully engineered heterostructures, our work demonstrates that illumination alone is sufficient to reconfigure the transport regime of a single-material device. In the dark, the transistor exhibits ambipolar characteristics with dominant n-type conduction, but under controlled optical excitation, it evolves into a clear anti-ambipolar profile. This light-driven transition is not only reversible and reproducible but also allows the definition of three distinct current states, enabling ternary logic operation without the need for complex heterojunction architectures. The peak current scales linearly with illumination intensity, showing that optical excitation provides a powerful handle for modulating device behavior. In this way, the same WSe_2 FET integrates logic functionality and photodetection within a compact platform, bridging computation and sensing. By shifting the focus from structural engineering to optical control, this concept establishes a versatile route for next-generation optoelectronic systems. The ability to tune transport regimes by light offers new degrees of freedom for designing reconfigurable, low-cost, and multifunctional circuits that combine speed, energy efficiency, and scalability.

Introduction

In recent decades, two-dimensional (2D) layered materials, particularly transition metal dichalcogenides (TMDs), have attracted widespread attention because of their unique and tuneable electrical and optical characteristics that make them appealing for next-generation optoelectronic and circuit applications.[1–6] In recent years, exploiting the absence of dangling bonds and the relaxed constraints on lattice matching, van der Waals (vdW) heterostructures have been fabricated by stacking different 2D layers of these materials with several methods. Developing beyond single material devices, these heterostructures have demonstrated significant potential in various technologies, including photodetection, transistor operation, sensing, logic devices and neural network applications.[7–11]

Building on these developments, 2D materials are now being considered for next-generation logic architectures in response to the growing demands of high-speed, compact, and flexible electronics driven by advances in artificial intelligence and neuromorphic computing. To meet these challenges, novel electronic and optoelectronic logic devices, such as ternary inverters, bipolar components,[12] and multi-level systems, are increasingly needed.

Recently, as a novel feature, anti-ambipolar behaviour, which contrasts with the more common ambipolar response,

[a] *Department of Physics "E. R. Caianiello", University of Salerno, via Giovanni Paolo II, Fisciano, Salerno, 84084, Italy. E-mail: kintonti@unisa.it, adibartolomeo@unisa.it*
[b] *CNR-SPIN Salerno, via Giovanni Paolo II, Fisciano, 84084, Italy*
[c] *Tyndall National Institute, University College Cork, Lee Maltings, Dyke Parade, Cork, T12 R5CP, Ireland*
[d] *School of Chemistry, University College Cork, Cork, Ireland*

was found in several 2D/2D heterostructures. Anti-ambipolar behaviour refers to the drain current reaching a local maximum at a specific gate voltage, which results in an ''Λ-shaped'' current *vs.* gate voltage curve rather than the typical ''V-shape'' of ambipolar devices. Devices based on this feature can implement numerous logic functions, such as having more than two logic states for information storage and information transmission, which are crucial to simplify the circuit design and increase their energy efficiency.

This phenomenon was first observed in carbon nanotubes/MoS_2 p–n heterojunctions[13] by Jariwala *et al.*, and it was attributed to the tunability, with gate bias, of the resistance of the p and n-type semiconductors in series, which affects the net series resistance of the channel.

More recently, anti-ambipolarity was investigated in 2D/2D p–n heterojunctions. The performance of these junctions depends largely on the threshold voltages of their respective p-type and n-type materials. The threshold voltage of the p material needs to be higher than the threshold voltage of the n material to have this feature, as highlighted by Li *et al.*[14] They fabricated p–n heterojunctions by using p-WSe_2, n-MoS_2 and n-SnS_2. Apart from choosing the right material combination, several improvement strategies, such as intentional doping and increasing carrier concentrations by using thicker TMDs, were discussed.

Accordingly, Sun *et al.*[15] combined a few-layer p-$MoTe_2$ with multi-layer n-InSe to obtain a type II band alignment, which results in an ''Λ'' shape of the transfer curve with a peak-to-valley ratio of 10^3. The quantum confinement effect and the strong interlayer coupling allow for modulating the bandgap and carrier concentration of 2D materials by changing their thickness. Therefore, the threshold voltage of the two components can be controlled separately by tuning the number of layers.

Lv *et al.*[16] found the anti-ambipolar behaviour at room temperature under both dark and illuminated conditions in a p-WSe_2/n-SnS_2 type II heterojunction. They analysed the phenomenon with an equivalent circuit model and simulations based on Poisson and drift-diffusion equations. Having a type-II heterojunction with doped n and p materials is not necessarily enough to observe anti-ambipolarism. It is needed to have a large vdW barrier at the interface, together with recombination of electrons and holes at the space charge region to have a strong peak-to-valley ratio.

Also, other combinations, such as p-$MoTe_2$/n-MoS_2[17] and BP/MoS_2,[18] have been discovered to show this feature under different conditions. However, it is still a challenge to fabricate anti-ambipolar devices with reliable and consistent performance, primarily because it requires a highly accurate control of the on-set voltage and the carrier density of both n-type and p-type components. Moreover, 2D/2D heterostructures strongly depend on precise interface quality and multi-layer fabrication processes that lead to high production costs and complexity, limiting practical deployment.

In the search for architectures based on a single material, WSe_2-based FETs have attracted significant attention. WSe_2 is a group-VI TMD that exhibits an indirect bandgap of 1.25 eV in its bulk form, which transitions to a direct bandgap of 1.64 eV in the monolayer limit. Unlike many other semiconductors, WSe_2 typically shows p-type or ambipolar transport behavior, making it particularly attractive for a variety of electronic and optoelectronic applications.[19]

Thakar and Lodha[20] demonstrated that ambipolar and anti-ambipolar transport in a WSe_2-based field-effect transistor can be reconfigured and tuned by using a dual electrostatic control scheme. Their device employs three back gates: one controls the channel region, while the other two, connected together, modulate the regions beneath the metal contacts, affecting the Schottky barriers. By adjusting the voltages applied to these two sets of gates, the polarity of each region can be independently controlled, enabling different transport regimes depending on the chosen bias configuration. This enables the realization of multi-bit encoding schemes. The physical mechanism is similar to that in p–n junction devices.

Simpler architectures were used by Wang *et al.*,[21] who fabricated a WSe_2-based field effect transistor with large Schottky barriers at the metal contact interfaces. Because of large barriers, under dark conditions, the transistor is in the off-state, but anti-ambipolar transport occurs under light illumination. Three logic states can be identified in the transfer curve under illumination by sweeping the gate bias.

In this study, we propose a back-gate WSe_2-based field effect transistor with Ni/Au metal contacts. Under dark conditions, the device shows a slight ambipolar behaviour with a dominant n-type conduction, which, under illumination, transforms into anti-ambipolar transport. The amplitude and position of the peak in the drain current are tunable by increasing the light intensity and the sweep delay in the measurement acquisition system. This phenomenon was investigated under both the illumination of a white LED ring and a monochromatic red laser. The light-induced transition from ambipolar to anti-ambipolar behaviour in WSe_2 provides multiple degrees of freedom, enabling precise tuning and control of different electronic states *via* gate voltage and/or illumination.

Experimental materials

WSe_2 flakes, whose atomic structure along three axes is displayed in Fig. 1a, were mechanically exfoliated by using scotch tape and successively transferred on a Si/SiO_2 (85 nm) substrate. Ni/Au (20 nm : 200 nm) metal contacts were deposited by metal evaporation and patterned through standard photolithography and lift-off processes, giving the device shown in the optical image in Fig. 1b. Raman spectra acquired from other devices fabricated using the same process, confirming the structural integrity and material quality of WSe_2, are shown in Fig. S1. The asymmetry in the contacts, arising from the different geometry, is considered potentially beneficial, as similar configurations have shown useful effects in WSe_2 devices.[22] The height profiles, acquired through atomic force microscopy (AFM) in contact mode, reveal that the multi-layer

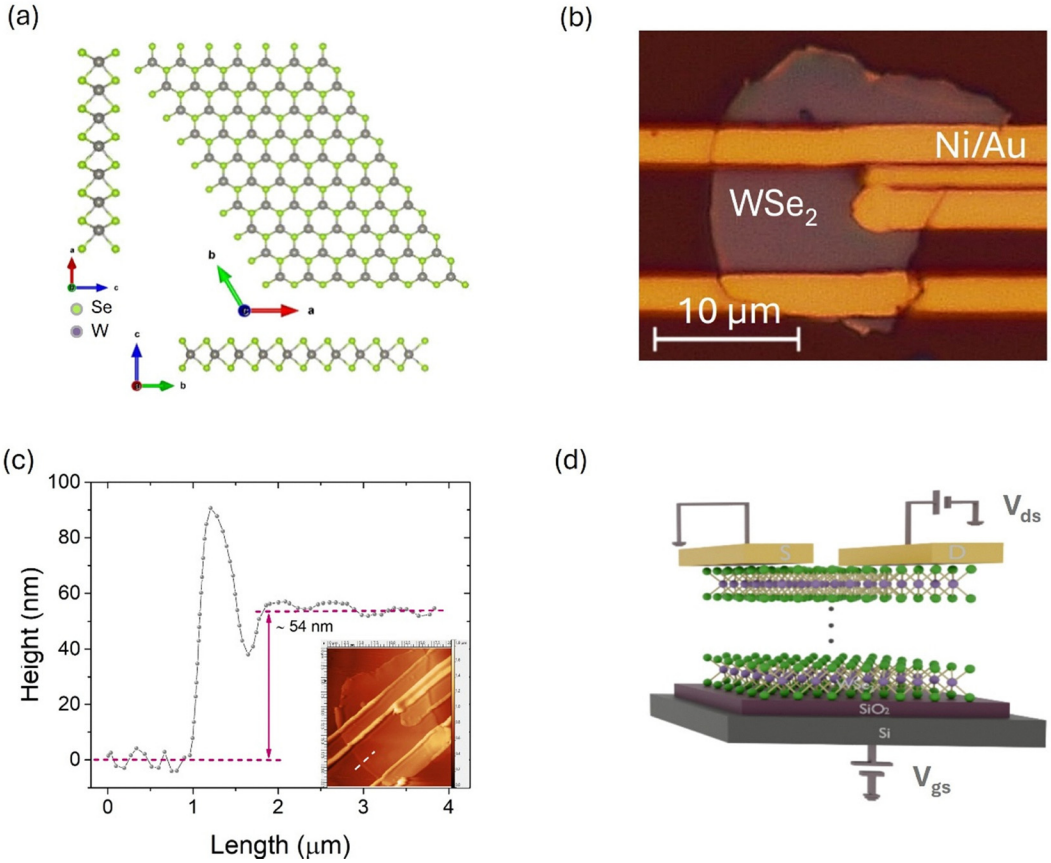

Fig. 1 (a) Atomic structure of WSe_2 along three axes. (b) Optical image of the WSe_2-based field effect transistor with Ni/Au metal contacts. (c) AFM profile extracted along the white line represented in the AFM image in the inset. (d) Schematic of the device showing the measurement set up.

flake is around 50 nm thick. A representative profile is shown in Fig. 1c. As mentioned above, thicker flakes enable higher carrier concentration than thinner flakes. The schematic of the device together with the measurement set up is displayed in Fig. 1d. We performed electrical measurements in a two-probe configuration using a Janis probe station equipped with nanoprobes connected to the source/drain leads. The back gate voltage was applied through the sample holder of the probe station that is in direct electrical contact with the substrate. The measurements were acquired through a Keithley 4200 SCS Parameter Analyzer at room temperature and pressure. The photoresponse of the device was investigated using a white LED ring with a maximum power of 1.4 W and a Thorlabs (639 nm) red laser with a nominal power of 4.37 mW.

Results and discussion

Section 1: Electrical characterization under dark conditions

We first performed electrical measurements in the dark. Fig. 2a shows the output curves (I_{ds} *vs.* V_{ds} as a function of V_{gs}) on a semi-log scale obtained by sweeping V_{ds} between −1 and 1 V and stepping V_{gs} from −20 to 20 V. At V_{gs} = 0 V, the deviation from linearity in the I_d–V_{ds} curve indicates the presence of Schottky barriers at the metal/WSe_2 interfaces.[23] The drain current is in the range of tens of pA, confirming that the contacts are highly resistive and that significant carrier injection requires applying a gate bias. We limited to ± 20 V the bias applied at the gate terminal to avoid stressing the gate oxide and because the current had already reached saturation within this range. Beyond the non-linear behaviour, the output curves are also asymmetric, revealing that the two metal/semiconductor interfaces contribute differently to charge injection. In particular, positive drain biases favor charge injection more effectively, consistent with asymmetric Schottky barriers at the source and drain.[24,25] This asymmetry is more pronounced at positive gate voltages. For clarity, band diagrams describing the evolution of the Schottky barriers under different gate conditions are included in Fig. S2. The drain current increases while stepping the gate bias both positively and negatively, revealing that the device shows a slight ambipolar behaviour.

The ambipolar conduction is confirmed by the transfer curves (I_d *vs.* V_{gs} at fixed V_{ds}) in Fig. 2b and c, acquired at positive and negative V_{ds}, respectively, by sweeping V_{gs} from 20 to −20 V. Ambipolarity is related to a band shift under the application of an external field, which is equivalent to displace the Fermi level between the valence band and the conduction band, which is possible because of the weak Fermi level pinning at the metal/WSe_2 interface. The effective polarity depends on the thickness of WSe_2 and the work function of

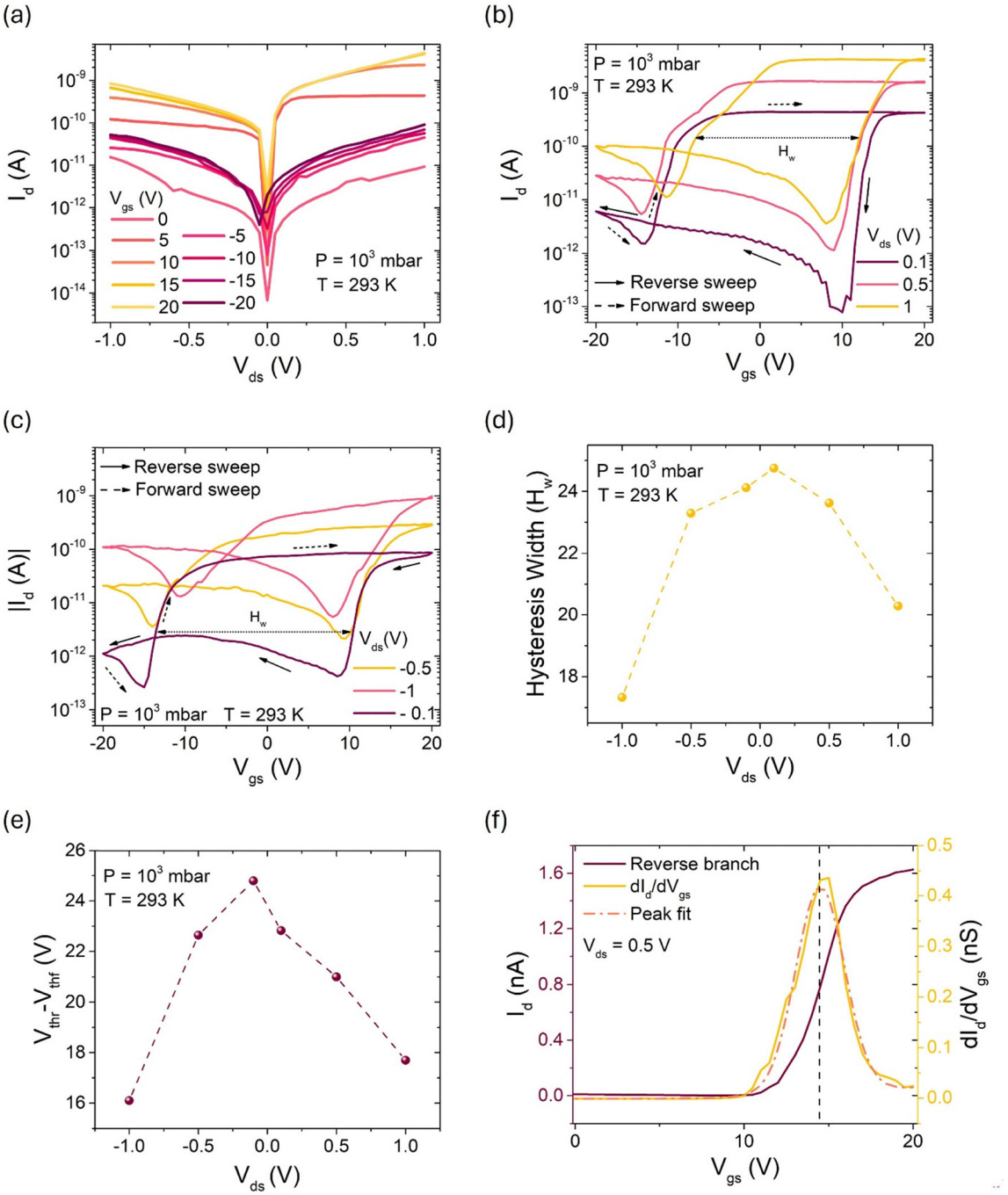

Fig. 2 (a) Output curves obtained by sweeping V_{ds} between −1 and 1 V at different gate voltages. (b) Transfer curves obtained by double sweeping V_{gs} between 20 and −20 V at several positive V_{ds} and (c) negative V_{ds}. (d) Extraction of the hysteresis width from the transfer curves reported in (b) and (c). (e) Extraction of the shift in the threshold voltage between the forward and the reverse branches of the transfer curves. (f) Identification of the maximum transconductance along the reverse branch of the transfer curve at V_{ds} = 0.5 V.

the metal contacts.[26,27] Ni contacts enable a transition from p-type transport for thin devices to ambipolar and then n-type behaviour as the WSe_2 thickness increases.[28] The dominant n-type behaviour in our device confirms that the Ni Fermi level is closer to the conduction band of the 50 nm thick WSe_2 and injects electrons more easily than holes.[29] The p-type behaviour, also induced by electronegative adsorbates on the surface of the material,[30,31] becomes more pronounced at higher V_{ds} since the barrier at the valence band becomes thinner.

The on-current I_{on} grows with V_{ds} both at the n and p-type sides, but this does not determine an increase in the I_{on}/I_{off} ratio of the device. For the n-side, it is about three orders of magnitude (10^3) at positive V_{ds} and two orders of magnitude at negative V_{ds}.

By double sweeping the gate bias, a wide hysteresis occurs, especially at the n-side. Because of the slight ambipolarity the device shows, it determines a butterfly shape in the transfer curve. The transition biases between n and p conduction, corresponding to the minimum I_d values in the transfer curves, exhibit a left shift along the reverse branch and a right shift along the forward branch, as V_{ds} increases in absolute value.

Hysteresis is predominantly due to the defective interface with the SiO_2 layer, but also to trapping mechanisms inside the material and surface-adsorbate-induced traps.[32] Measurements performed in high vacuum, indeed, reveal a narrower hysteresis.[33] Under an increasing positive gate voltage (forward sweep), the acceptor traps capture electrons, so that they can act as an additional negative gate bias during the application of a decreasing V_{gs} (reverse sweep). This produces a right shift of the threshold voltage on the reverse branch.[34] The hysteresis width, extracted as the maximum voltage distance between the reverse and forward branches, and reported in Fig. 2d, increases from $\sim$17 to 24 as V_{ds} goes from -1 to -0.1 V and lowers from $\sim$25 to 20 V as V_{ds} increases from 0.1 to 1 V. The threshold voltage can be determined by finding the intersection between the *x*-axis and the linear fit of the initial (lower) portion of the transfer curve, at the onset of conduction. The separation between the threshold voltage on the reverse branch V_{thr} and on the forward branch V_{thf}, consistently decreases as $|V_{ds}|$ increases, ranging from 22 to 16 V at positive V_{ds} and from 24 to 16 V at negative ones, see Fig. 2e.

The maximum mobility is calculated using the following formula:

$$\mu = g_m \frac{L}{C_{ox} W V_{ds}}$$

where g_m is the maximum transconductance, L and W are the length and width of the channel and $C_{ox} = 4.06 \times 10^{-8}$ F cm^{-2} is the oxide capacitance per unit area. The electron mobility is higher than the hole one and reaches its maximum at positive V_{ds} in correspondence with the inflexion point of the reverse branch, as pointed out by Fig. 2f for the V_{ds} = 0.5 V case. However, the mobility is quite low, the maximum being around $(9 \pm 2) \times 10^{-3}$ cm^2 V^{-1} s^{-1}. It is likely limited by scattering events with the defects of the material,[35] surface states and mainly at the interface with the oxide,[36] as suggested by the hysteresis. The slight variations in FET electrical parameters for positive and negative V_{ds}, including on-current, on/off ratio, mobility, and hysteresis width, support the presence of asymmetric Schottky barriers, likely due to unequal metal contact areas that cause different contact resistances at the metal interfaces.[25]

Section 2: Electrical characterization under LED light

The photoresponse of the device was first recorded under the illumination of a white LED ring (400–700 nm), providing broadband illumination across the visible light range, where WSe_2 exhibits high optical absorption.[37] This allows a comprehensive evaluation of the device's behaviour under visible-light excitation, without biasing the measurement toward a specific wavelength. The *I*–*V* curve at V_{gs} = 0 V in Fig. 3a shows a significant enhancement of the drain current when the light is on at both positive and negative V_{ds}. To investigate the impact of the gate bias on the drain current, we measured transfer curves under light by double sweeping V_{gs} from 20 to -20 V. To emphasize the differences between the transfer characteristics under dark and illuminated conditions, a direct comparison is presented. For the sake of clarity, the analysis is restricted to V_{ds} = 0.5 V and -0.5 V, see Fig. 3b and c, respectively, but the analogous behaviour is observed at different V_{ds}.

Under illumination, the device exhibits positive photoconductivity across all gate voltages, resulting in an overall upward shift of the transfer curve compared to the dark condition. However, ambipolar transport develops into a more complex scenario, as the gate voltage modulates the channel current to produce distinct peaks at specific gate biases, indicating the onset of anti-ambipolar behavior at both positive and negative V_{ds}.

The transfer curves under illumination also exhibit hysteresis. Two separate current peaks appear during the gate voltage double sweep at fixed V_{ds}: one along the reverse sweep at positive gate voltages and the other along the forward sweep at negative gate voltages.

In Fig. 3d, the reverse branches (solid lines) of the transfer curves at $V_{ds} = -0.5$ V and 0.5 V are separately shown and three distinct operating regions can be identified as a function of the gate bias. (The same for the forward sweep is reported in Fig. S3). Moving from left to right, the current initially remains nearly constant for $V_{gs} < 2$ V (yellow region), with a gentle decreasing slope as V_{gs} increases, resembling the p-type branch of the transfer curve in the dark. The peaked regions, instead, extend between $\sim$2 and 12.5 V (orange region). At positive V_{ds}, the current of the peak follows the shape of the transfer curve: the current level on the right side of the peak is higher than on the left, and the peak maximum does not correspond to the highest current value in the transfer curve. Conversely, the peak observed at negative V_{ds} shows the opposite trend, with the current on its right side lower than on the left, and it is more pronounced than in the positive counterpart. For $V_{gs} > 12$ V (pink region), the current enters a monotonically increasing region, resembling the *n*-branches of the dark transfer curves, and approaches saturation at positive V_{ds}.

Anti-ambipolar transport naturally gives rise to negative differential resistance (NDR), a nonlinear carrier transport phenomenon in which increasing the bias voltage leads to a reduction in current. Various architectures have been exploited to obtain it in TMD-based structures. For instance, Wang *et al.*[38] identified semiconducting TMDs hosting the S-type NDR in a vertical electrode/TMD/electrode structure, and they attributed it to the thermal feedback conduction mechanism induced by the Joule self-heating effect. Huo *et al.*,[39] instead, proposed a VdW heterostructure made of semi-metallic Td-WTe_2 and $MoS_2/MoTe_2$, exploiting the formation of a type-III band alignment. In both cases, the NDR appears as a peak in the *I*–*V* characteristics. In our case, anti-ambipolar transport manifests as negative transconductance (NTC) with respect to the gate voltage, see the dashed lines in Fig. 3d. Such a feature

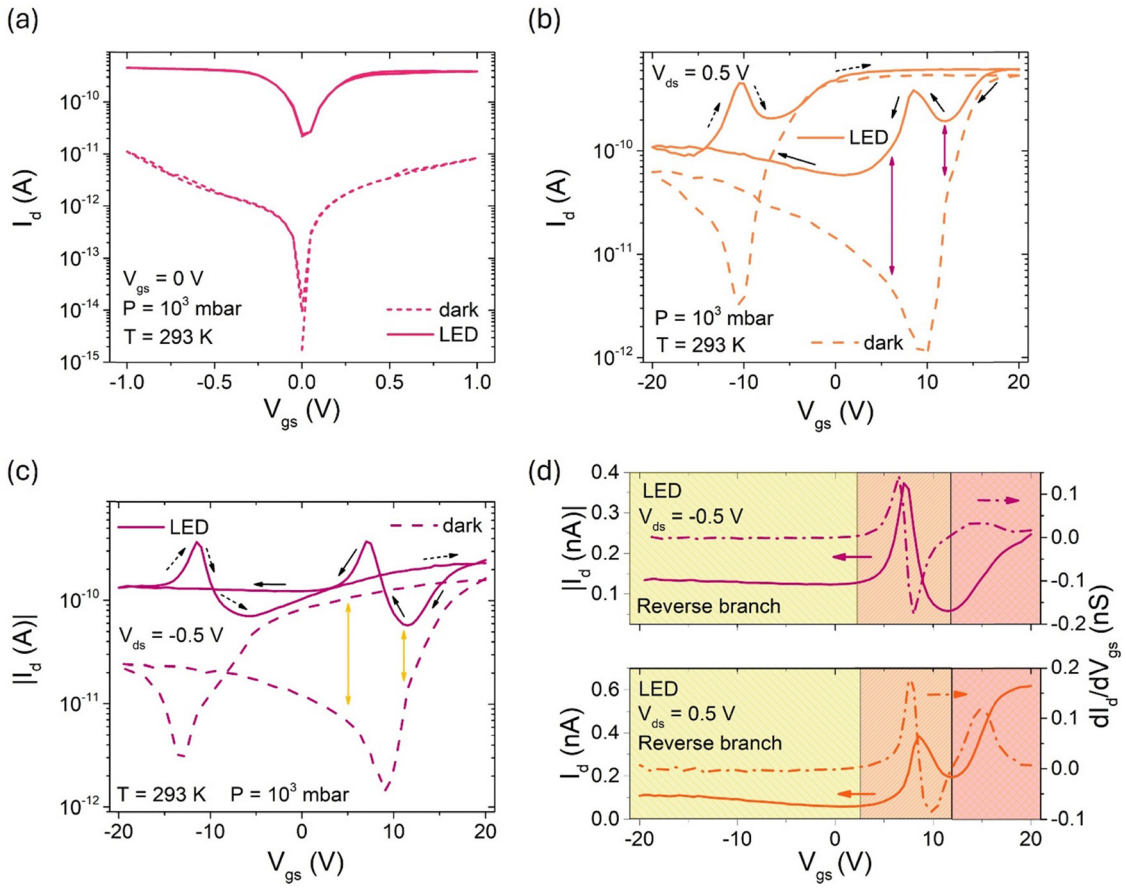

Fig. 3 Comparison between (a) I_d–V_{ds} curves, (b) transfer curves at V_{ds} = 0.5 V, and (c) transfer curves at V_{ds} = −0.5 V, measured in the dark and under LED illumination. Colored arrows highlight the alignment between the inflection points of the dark transfer curves and the onset of the peak photoresponse. (d) The three colored regions identify distinct operating regimes along the reverse sweep (solid lines) of the transfer curves at V_{ds} = −0.5 V (top) and V_{ds} = 0.5 V (bottom). Dashed lines represent the transconductance as a function of gate voltage in each case.

is valuable for various emerging analog and digital applications. In the analog domain, it has been shown that single material-based transistors exhibiting the coexistence of positive and negative transconductance regions can generate in-phase, out-of-phase, and frequency-doubled signals when an AC input on the gate terminal is combined with a proper DC bias.[37] Additionally, in some anti-ambipolar architectures, the interplay between gate biasing and optical modulation has been employed to produce phase-, amplitude-, and frequency-selective output waveforms, suitable for analog modulation/encoding schemes in data communications. Multi-bit analog transmission has also been demonstrated in transistor designs that allow switching between ambipolar and anti-ambipolar transport by electrostatically control drain/source barriers and channel polarity.[20] Furthermore, NTC has been exploited to realize ternary inverters and ternary static random access memory.[16,40,41]

Fig. 4a and b show the reverse and forward branches of the transfer curve at V_{ds} = −0.5, respectively, under progressively stronger illumination, from 0.18 to 1.1 W. The peaks already appear at low power and get sharper with increasing intensity. At low light intensity, a dip in the current close to the maximum peak is observed along both branches; however, as the intensity increases, only one peak remains visible. Something similar was observed in the $MoTe_2$–MoS_2 heterojunction, where the dip in the transconductance was related to photodoping.[42] We refer to the peak on the reverse branch as p1 and the one on the forward branch as p2.

The height of the peaks evaluated with respect to the baseline is almost the same on the two branches at fixed LED intensity. It ranges from $(3.2 \pm 0.2) \times 10^{-2}$ to $(2.46 \pm 0.08) \times 10^{-1}$ nA for p1, and from $(4.4 \pm 0.3) \times 10^{-2}$ to $(2.42 \pm 0.06) \times 10^{-1}$ nA for p2, as the LED intensity increases. This value is different from the maximum current, which is slightly higher and reaches 0.31 nA, as evident from Fig. 4a and b. When plotting the peak height as a function of the LED power, we observe a linear relationship for both p1 and p2, as indicated by the full symbols in Fig. 4c. The bias voltages at which p1 and p2 appear are indicated as V_{p1} and V_{p2} in Fig. S4. As the illumination increases, the position of p1 shifts slightly to the left, because of phototrapping processes, while V_{p2} remains nearly unchanged.

The driving voltage range (ΔV_g), defined as the voltage difference between the on-set and off-set of the peak, is narrower in our device compared to other reported devices and heterostructures,[15,43] where ΔV_g typically spans several tens of volts. In our ambipolar channel, this range corresponds to the

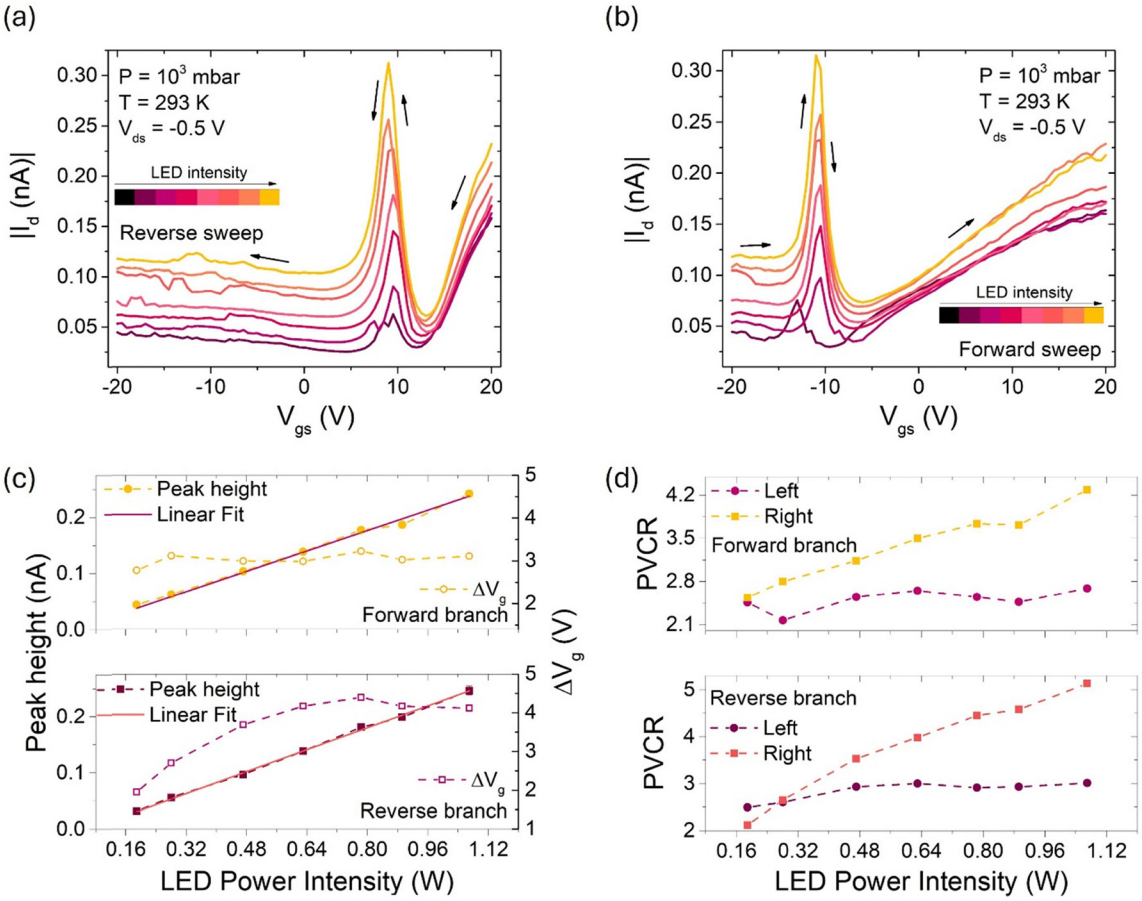

Fig. 4 (a) Transfer curve under LED light obtained by reverse sweeping and (b) forward sweeping the gate bias at $V_{ds} = -0.5$ V. (c) Amplitude of the peaks (left scale) and driving voltage range (right scale) extracted from the forward branch (top) and reverse branch (bottom) as a function of the LED power intensity. (d) Peak-to-valley current ratio calculated on the forward branch (top) and the reverse branch (bottom) considering the left side (square) and the right side (circle) of the peak.

bias region where both p- and n-type conduction branches are partially active; outside this region, one mode dominates. Inflection points in the dark curves align with the onset of the photoresponse peak, as indicated by the colored arrows in Fig. 3b and c, reflecting the overlap of the initial, resistive portions of both branches. This reduced ΔV_g is favourable since it enables faster and more energy-efficient switching in logic circuits.[41,44] In our measurements, ΔV_g is almost constant around 3 V in the forward sweep, while it can be tuned from approximately 2 to 4 V in the reverse sweep – see empty symbols in Fig. 4c. The full width at half maximum (FWHM) of the forward peaks, indeed, are lower than the peaks on the reverse branch.

The peak-to-valley current ratio (PVCR) is not the same as the peak is approached from the left or from the right, because of the transfer curve shape, as highlighted in Fig. 4d for both the reverse and the forward branches. At the maximum LED intensity, it reaches approximately 4 on the forward branch and $\sim$5 on the reverse branch, which is lower than in heterostructures, but comparable with other WSe_2-based devices.[21] However, it needs to be improved for efficient applications.

Table S1 compares the main figures of merit of our device with those reported in the literature.

Section 3: Electrical characterization under a red laser

To gain deeper insight into the phenomenon, the device's photoresponse was also investigated under illumination with a monochromatic red laser ($\lambda \approx 639$ nm), corresponding to a photon energy of approximately 1.94 eV. This energy lies above the WSe_2 bandgap ($\sim$1.2–1.7 eV),[45] enabling efficient photocarrier generation while avoiding high-energy induced effects. Red excitation is also standard in WSe_2 photodetector studies. The drain current significantly increases, see Fig. 5a, by three orders of magnitude from the dark one. Fig. 5b compares the transfer characteristics in the dark and under light, at $V_{ds} = -0.5$ V.

The overall behaviour is the same as under white light, but with a higher photocurrent. However, unlike the case under LED illumination, the forward and reverse branches of the curve can be sharply divided into three distinct current regions, as highlighted in Fig. 5c at $V_{ds} = -0.5$ V. The same applies at positive V_{ds}, see Fig. S5. In both cases, in the yellow and pink regions, the gate bias barely modulates the drain current, which remains at two flat levels. This behaviour is due to the

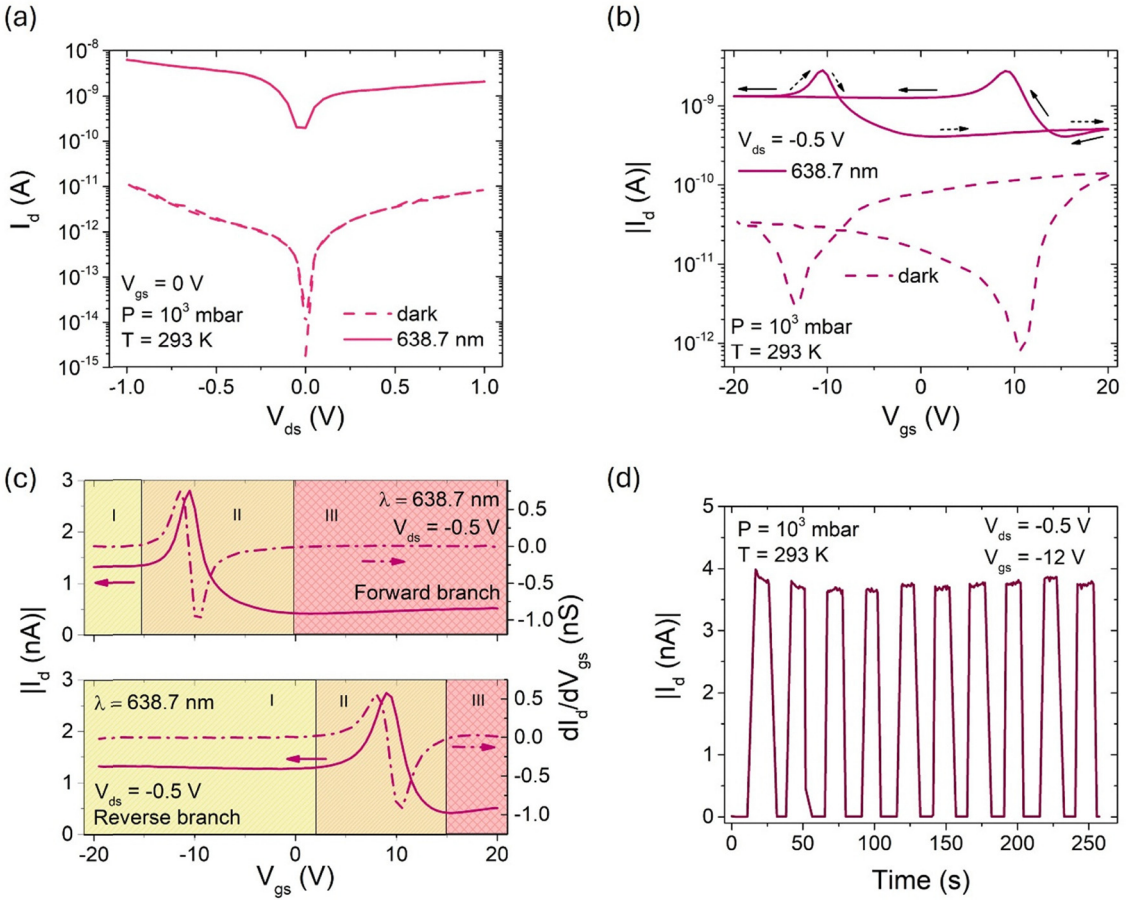

Fig. 5 Comparison between (a) the I–V curves and (b) the transfer curves at $V_{ds} = -0.5$ V in the dark and under red laser illumination. (c) Identification of three separate current levels (solid lines) in the forward (top) and reverse (bottom) branches of the transfer curves. Dashed lines represent the transconductance. (d) Switching behaviour of the device in response to repeated laser pulses, in correspondence to the peak on the forward branch.

laser's higher local power density and spatial confinement, which generate a large concentration of carriers in a small region, locally lowering the Schottky barriers and enhancing injection. As a result, the current becomes less sensitive to gate modulation, leading to flatter response levels. Nevertheless, a prominent peak appears in the central region despite the overall saturated regime, and the peak current is the highest obtained when sweeping the gate bias both at $V_{ds} = -0.5$ and 0.5 V. The values of V_p and the driving voltage range ΔV_{gs} are consistent with those obtained under LED illumination.

In both branches, in Fig. 5c, the current in region I is approximately 1.33 nA, reaches a peak of 2.8 nA, and then drops to about 0.4 nA in region III. These three current levels are stable and well-defined, suggesting that the device can operate as a multi-level element under controlled illumination conditions. Multi-state devices are particularly attractive for circuit miniaturization because they can encode more information per device than binary CMOS. Whereas CMOS logic requires at least two transistors to encode a single bit, a ternary logic unit provides three distinct output states, increasing information density from 2^n to 3^n levels with the same number of units.

Considering that the peaks in the transfer curve under illumination almost coincide with the valley in the ambipolar transfer curves in the dark, we investigated the dark-light switching behaviour of the device at $V_{gs} = V_{p2}$ as this gate voltage provides the largest separation between the current values measured in the dark and under illumination. The current increases quickly, reaching a steady on-state current and then decreases rapidly when the light is switched off, indicating a rapid photodetection mechanism at this bias point. From the pulses in Fig. 5d, we extracted the photocurrent as:[46]

$$I_{ph} = I_{light} - I_{dark} = (3.73 \pm 0.07)\ \text{nA}$$

Defining $P_{inc} = (P/A_{spot})\cdot A_{flake}$ as the incident power and q as the electron charge, we can calculate the responsivity as follows:

$$R = \frac{I_{ph}}{P_{inc}} \approx 0.13\frac{A}{W}$$

and the detectivity as:

$$D^* = R\sqrt{\frac{A_{flake}}{2qI_{dark}}} \approx 1.3 \times 10^{12}\text{Jones}$$

During operation with 10-second light pulses, the instantaneous power consumption in the ON state is ~1.85 nW, while

in the dark state it drops to ~1 pW. The average power dissipation over a full light–dark cycle is below 1 nW:

$$P_{avg} = \frac{V_{ds} I_{light} t_{on} + V_{ds} I_{dark} t_{off}}{t_{on} + t_{off}} \sim 0.93\,\text{nW}$$

Additionally, the narrow driving voltage range minimizes the dynamic power consumption. All these parameters highlight the anti-ambipolar transistor's promise for low-power optoelectronics.

Section 4: Mechanism

Based on the direct comparison between the transfer curves in the dark and under illumination presented in the previous section, we observe that the on-set gate bias of ambipolarity in the dark is linked with the current peak under light. Specifically, the vertex of the V-shaped ambipolar transfer curve in the dark is related to the peak of the Λ-shaped anti-ambipolar transfer characteristic under illumination.

The correspondence between the two points is not precise because the acquisition time for the transfer curves in the dark and under illumination differs. Even with identical measurement settings, the time required to record each data point depends on the current level: lower currents, as typically observed in the dark, result in longer measurement times.

Therefore, we tried to slow down the measurement in light by adding a sweep delay (see Fig. S6) at each data point acquisition time. Under these conditions, p1 on the reverse sweep shifts to higher gate voltages, while p2 on the forward sweep shifts to lower gate voltages. This indicates that, during both reverse and forward V_{gs} sweeps, reducing the sweep speed causes the peaks to appear earlier along the gate voltage axis and they better align with the minimum points of the transfer curves in the dark. This result supports our hypothesis that anti-ambipolar peaks correspond to the ambipolar transition points.

In the dark, the drain current can be described as the sum of electron and hole contributions, each enabled by thermionic emission and tunneling through a gate dependent Schottky barrier. The dominant n-type behaviour observed in Fig. 2 indicates that the energy barrier for electrons injection is lower than the hole barrier. As illustrated in Fig. 6a, for $V_{gs} > V_p$, the electron barrier at the source becomes thinner, enhancing n-type conduction, while for $V_{gs} < V_p$, upward band bending at the drain side reduces the hole barrier, enabling the p-type transport (Fig. 6b).[29] At $V_{gs} = V_p$, both barriers are sufficiently large to suppress the injection of either carrier type, resulting in the minimum in the transfer curve (Fig. 6c). As already mentioned, this minimum defines the transition point between n-type and p-type conduction. A small deviation from this gate voltage enables either n-type or p-type transport, depending on

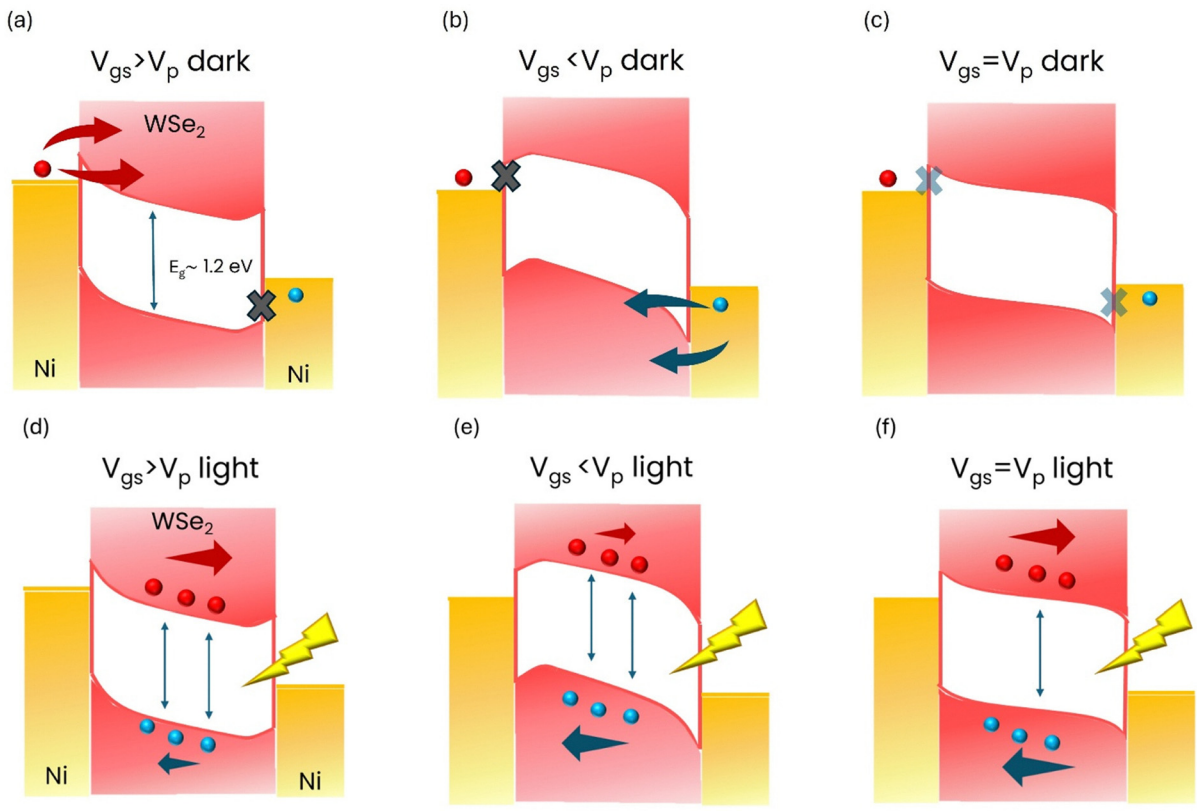

Fig. 6 Band diagrams showing the band bending at the source–drain interfaces and along the channel together with the current transport in the dark at (a) $V_{gs} > V_p$, (b) $V_{gs} < V_p$, and (c) $V_{gs} = V_p$. (d)–(f) The same under illumination.

the direction of the sweep. This behavior is typical of Schottky-contact transistors, where carrier injection is strongly modulated by gate-controlled band bending.

Under illumination, photogenerated electron–hole pairs modify the device operation, see Fig. 6d–f. At gate voltages far from V_p, the device remains largely unipolar: either photoelectrons ($V_g > V_p$) or photo-holes ($V_g < V_p$) dominate the photocurrent, as the opposite carrier faces higher injection barriers and recombination processes. In contrast, around $V_{gs} = V_p$, the band structure let both photogenerated carriers to be transferred and collected efficiently as illustrated in Fig. 6f: photoelectrons can flow to the drain and holes to the source, and their simultaneous collection produces a pronounced local maximum, giving rise to the characteristic Λ shaped anti-ambipolar response. When the gate bias is at the n–p crossover, both Schottky barriers are moderately high, too high for thermal injections, but not so high to impede photogenerated carriers' transport.

Thus, the observed light-induced anti-ambipolar peak results from the combined effects of dual Schottky barrier modulation at source and drain and efficient photogeneration and separation of both carrier types across the flake at V_p enabled by a proper band alignment. This scenario is supported by previous reports of anti-ambipolarity in both heterojunctions and multilayer homostructures and confirms the capacity of bulk WSe_2 to host multi-state transport under optical stimulation.

Conclusions

In this work, we investigated the electrical properties of a multilayer WSe_2 based field-effect transistor, studied at room temperature and ambient pressure, both in the dark and under illumination with two different light sources. In the dark, the device exhibits ambipolar behaviour with dominant electron conduction and a characteristic butterfly-shaped transfer curve due to pronounced hysteresis. Upon illumination, the drain current increases overall but shows a peak at specific gate voltages, indicating a transition to anti-ambipolar behaviour. The amplitude of this peak can be modulated by the light intensity, and the narrow driving voltage range makes the device promising for fast switching circuits. The resulting peak-to-valley ratio is such that three distinct logic states can be distinguished, particularly under illumination with a collimated red laser. Notably, the peak in the transfer curve under illumination appears near the valley of the dark ambipolar curve, prompting a closer examination of the transient response at this point. The resulting measurements highlight promising photodetection performance and qualitative energy band diagrams are used to describe and suggest the origin of the observed transition. A systematic thickness-dependent study was not performed in this work; however, it is well established that the electrical properties of WSe_2, such as mobility, carrier type and density, screening, and Schottky barrier height, vary significantly with layer number.[28,47] Additionally, because WSe_2 exhibits relatively weak Fermi-level pinning, the balance between electron and hole injection and the position of the n–p transition point are also influenced by the alignment between the metal work function and the WSe_2 band structure.[29] Since the light-induced anti-ambipolar peak observed here is linked to this n → p crossover, variations in thickness are expected to influence whether the transition appears and at which gate voltage it occurs. These considerations suggest that a dedicated, thickness-dependent study could offer valuable insight into the tunability of the anti-ambipolar effect and may be pursued in future investigation.

Conflicts of interest

There are no conflicts to declare.

Data availability

The data supporting the findings of this study are available from the corresponding authors upon reasonable request.

The data supporting this article have been included as part of the supplementary information (SI). The supplementary information contains Raman spectra, additional band diagrams providing qualitative insight into the device behaviour, measurements performed under different biasing and sweep-delay conditions, and a comparative table with previously reported works. See DOI: https://doi.org/10.1039/d5mh01871d.

Acknowledgements

A. D. B. acknowledges funding from the University of Salerno through project ORSA254881. This work was partially supported by the Research Ireland (formerly Science Foundation Ireland) AMBER Research Centre (SFI-12/RC/2278_P2). V. P. acknowledges funding from the EU-MSCA project 101153933.

References

1 K. Intonti, E. Faella, A. Kumar, L. Viscardi, F. Giubileo, N. Martucciello, H. T. Lam, K. Anastasiou, M. Craciun, S. Russo and A. Di Bartolomeo, Temperature-Dependent Conduction and Photoresponse in Few-Layer ReS2, *ACS Appl. Mater. Interfaces*, 2023, **15**(43), 50302–50311, DOI: 10.1021/acsami.3c12973.

2 F. Qian, X. Bu, J. Wang, J.-Y. Mao, S.-T. Han and Y. Zhou, Transistors and Logic Circuits Enabled by 2D Transition Metal Dichalcogenides: A State-of-the-Art Survey, *J. Mater. Chem. C*, 2022, **10**(45), 17002–17026, DOI: 10.1039/D2TC00964A.

3 L. Viscardi, E. Faella, K. Intonti, F. Giubileo, V. Demontis, D. Prete, V. Zannier, L. Sorba, F. Rossella and A. Di Bartolomeo, Temperature Behavior and Logic Circuit Applications of InAs Nanowire-Based Field-Effect Transistors, *Mater. Sci. Semicond. Process.*, 2024, **173**, 108167, DOI: 10.1016/j.mssp.2024.108167.

4 A. Kumar, K. Intonti, L. Viscardi, O. Durante, A. Pelella, O. Kharsah, S. Sleziona, F. Giubileo, N. Martucciello, P. Ciambelli, M. Schleberger and A. D. Bartolomeo, Memory Effect and Coexistence of Negative and Positive Photoconductivity in Black Phosphorus Field Effect Transistor for Neuromorphic Vision Sensors, *Mater. Horiz.*, 2024, **11**(10), 2397–2405, DOI: 10.1039/D4MH00027G.

5 A. Pelella, K. Intonti, O. Durante, A. Kumar, L. Viscardi, S. De Stefano, P. Romano, F. Giubileo, H. Neill, V. Patil, L. Ansari, B. Roycroft, P. K. Hurley, F. Gity and A. Di Bartolomeo, Multilayer WS2 for Low-Power Visible and near-Infrared Phototransistors, *Discover Nano*, 2024, **19**(1), 57, DOI: 10.1186/s11671-024-04000-0.

6 A. Pelella; P. Romano; K. Intonti; L. Viscardi; O. Durante; D. Capista; M. Passacantando; F. Giubileo; M. A. S. Alshehri; M. S. G. Alghamdi; M. Craciun; S. Russo and A. D. Bartolomeo Optoelectronic Properties of Two-Dimensional α-In2Se3 Field Effect Transistor. In 2023 IEEE Nanotechnology Materials and Devices Conference (NMDC); 2023; 270–271, DOI: 10.1109/NMDC57951.2023.10344214.

7 S.-J. Liang, B. Cheng, X. Cui and F. Miao, van der Waals Heterostructures for High-Performance Device Applications: Challenges and Opportunities, *Adv. Mater.*, 2020, **32**(27), 1903800, DOI: 10.1002/adma.201903800.

8 L. Viscardi, A. Mazzotti, O. Durante, T. Pucher, N. Martucciello, A. Castellanos-Gomez and A. Di Bartolomeo, van der Waals WS2/PdSe2 Heterostructure as a Visible-Light Photodetector and Pressure Optoelectronic Sensor, *2D Mater.*, 2025, **12**, 045003, DOI: 10.1088/2053-1583/ade9da.

9 H. Xu, Y. Xue, Z. Liu, Q. Tang, T. Wang, X. Gao, Y. Qi, Y. P. Chen, C. Ma and Y. Jiang, van der Waals Heterostructures for Photoelectric, Memory, and Neural Network Applications, *Small Sci.*, 2024, **4**(4), 2300213, DOI: 10.1002/smsc.202300213.

10 O. Durante, S. De Stefano, A. Mazzotti, L. Viscardi, F. Giubileo, O. Kharsah, L. Daniel, S. Sleziona, M. Schleberger and A. Di Bartolomeo, Pressure-Dependent Current Transport in Vertical BP/MoS2 Heterostructures, *Heliyon*, 2025, **11**(3), e42443, DOI: 10.1016/j.heliyon.2025.e42443.

11 L. Viscardi, O. Durante, S. De Stefano, K. Intonti, A. Kumar, A. Pelella, F. Giubileo, O. Kharsah, L. Daniel, S. Sleziona, M. Schleberger and A. Di Bartolomeo, Dominant N-Type Conduction and Fast Photoresponse in BP/MoS2 Heterostructures, *Surf. Interfaces*, 2024, **49**, 104445, DOI: 10.1016/j.surfin.2024.104445.

12 J. Han, W. Deng, F. Hu, S. Han, Z. Wang, Z. Fu, H. Zhou, H. Yu, J. Gou and J. Wang, 2D Materials-Based Photodetectors with Bi-Directional Responses in Enabling Intelligent Optical Sensing, *Adv. Funct. Mater.*, 2025, **35**(24), 2423360, DOI: 10.1002/adfm.202423360.

13 D. Jariwala, V. K. Sangwan, C.-C. Wu, P. L. Prabhumirashi, M. L. Geier, T. J. Marks, L. J. Lauhon and M. C. Hersam, Gate-Tunable Carbon Nanotube–MoS_2 Heterojunction p-n Diode, *Proc. Natl. Acad. Sci. U. S. A.*, 2013, **110**(45), 18076–18080, DOI: 10.1073/pnas.1317226110.

14 Y. Li, Y. Wang, L. Huang, X. Wang, X. Li, H.-X. Deng, Z. Wei and J. Li, Anti-Ambipolar Field-Effect Transistors Based On Few-Layer 2D Transition Metal Dichalcogenides, *ACS Appl. Mater. Interfaces*, 2016, **8**(24), 15574–15581, DOI: 10.1021/acsami.6b02513.

15 Y. Sun, W. Gao, X. Li, C. Xia, H. Chen, L. Zhang, D. Luo, W. Fan, N. Huo and J. Li, Anti-Ambipolar Behavior and Photovoltaic Effect in p-MoTe2/n-InSe Heterojunctions, *J. Mater. Chem. C*, 2021, **9**(32), 10372–10380, DOI: 10.1039/D1TC02497C.

16 Y. Lv, C.-Y. Wu, Y. Zhao, G. Wu, M. Abid, J. Cho, M. Choi, Ó. C. Coileáin, K.-M. Hung, C.-R. Chang, Y.-R. Wu and H.-C. Wu, Robust Anti-Ambipolar Behavior and Gate-Tunable Rectifying Effect in van der Waals p–n Junctions, *ACS Appl. Electron. Mater.*, 2022, **4**(11), 5487–5497, DOI: 10.1021/acsaelm.2c01120.

17 A. K. Paul, M. Kuiri, D. Saha, B. Chakraborty, S. Mahapatra, A. K. Sood and A. Das, Photo-Tunable Transfer Characteristics in $MoTe_2$–MoS_2 Vertical Heterostructure, *npj 2D Mater. Appl.*, 2017, **1**(1), 17, DOI: 10.1038/s41699-017-0017-3.

18 M. Huang, S. Li, Z. Zhang, X. Xiong, X. Li and Y. Wu, Multifunctional High-Performance van der Waals Heterostructures, *Nat. Nanotechnol.*, 2017, **12**(12), 1148–1154, DOI: 10.1038/nnano.2017.208.

19 Q. Cheng, J. Pang, D. Sun, J. Wang, S. Zhang, F. Liu, Y. Chen, R. Yang, N. Liang, X. Lu, Y. Ji, J. Wang, C. Zhang, Y. Sang, H. Liu and W. Zhou, WSe2 2D P-Type Semiconductor-Based Electronic Devices for Information Technology: Design, Preparation, and Applications, *InfoMat*, 2020, **2**(4), 656–697, DOI: 10.1002/inf2.12093.

20 K. Thakar and S. Lodha, Multi-Bit Analog Transmission Enabled by Electrostatically Reconfigurable Ambipolar and Anti-Ambipolar Transport, *ACS Nano*, 2021, **15**(12), 19692–19701, DOI: 10.1021/acsnano.1c07032.

21 H. Wang, W. Gao, P. Wen, H. Yu, Y. Huang, Q. Yue, X. Wang and N. Huo, Light-Regulated Anti-Ambipolar Transport with Multi-Logic States in Metal-WSe_2-Metal Transistor, *Adv. Electron. Mater.*, 2022, **8**(12), 2200649, DOI: 10.1002/aelm.202200649.

22 C. Zhou, S. Zhang, Z. Lv, Z. Ma, C. Yu, Z. Feng and M. Chan, Self-Driven WSe_2 Photodetectors Enabled with Asymmetrical van der Waals Contact Interfaces, *npj 2D Mater. Appl.*, 2020, **4**(1), 1–9, DOI: 10.1038/s41699-020-00179-9.

23 A. Grillo and A. Di Bartolomeo, A Current–Voltage Model for Double Schottky Barrier Devices, *Adv. Electron. Mater.*, 2021, **7**(2), 2000979, DOI: 10.1002/aelm.202000979.

24 S. De Stefano, A. Spuri, R. Barbella, O. Durante, A. Mazzotti, A. Sessa, A. Di Bernardo and A. Di Bartolomeo, Multilayer MoS2 Schottky Barrier Field Effect Transistor, *IEEE Open J. Nanotechnol.*, 2025, **6**, 51–57, DOI: 10.1109/OJNANO.2025.3553692.

25 A. Di Bartolomeo, A. Grillo, F. Urban, L. Iemmo, F. Giubileo, G. Luongo, G. Amato, L. Croin, L. Sun, S.-J. Liang and L. K. Ang, Asymmetric Schottky Contacts in Bilayer MoS2

Field Effect Transistors, *Adv. Funct. Mater.*, 2018, **28**(28), 1800657, DOI: 10.1002/adfm.201800657.

26 Z. Wang, Q. Li, Y. Chen, B. Cui, Y. Li, F. Besenbacher and M. Dong, The Ambipolar Transport Behavior of WSe2 Transistors and Its Analogue Circuits, *NPG Asia Mater.*, 2018, **10**(8), 703–712, DOI: 10.1038/s41427-018-0062-1.

27 P. R. Pudasaini, A. Oyedele, C. Zhang, M. G. Stanford, N. Cross, A. T. Wong, A. N. Hoffman, K. Xiao, G. Duscher, D. G. Mandrus, T. Z. Ward and P. D. Rack, High-Performance Multilayer WSe2 Field-Effect Transistors with Carrier Type Control, *Nano Res.*, 2018, **11**(2), 722–730, DOI: 10.1007/s12274-017-1681-5.

28 C. Zhou, Y. Zhao, S. Raju, Y. Wang, Z. Lin, M. Chan and Y. Chai, Carrier Type Control of WSe2 Field-Effect Transistors by Thickness Modulation and MoO3 Layer Doping, *Adv. Funct. Mater.*, 2016, **26**(23), 4223–4230, DOI: 10.1002/adfm.201600292.

29 S. Das and J. Appenzeller, WSe2 Field Effect Transistors with Enhanced Ambipolar Characteristics, *Appl. Phys. Lett.*, 2013, **103**(10), 103501, DOI: 10.1063/1.4820408.

30 E. Faella, K. Intonti, L. Viscardi, F. Giubileo, A. Kumar, H. T. Lam, K. Anastasiou, M. F. Craciun, S. Russo and A. Di Bartolomeo, Electric Transport in Few-Layer ReSe2 Transistors Modulated by Air Pressure and Light, *Nanomaterials*, 2022, **12**(11), 1886, DOI: 10.3390/nano12111886.

31 F. Urban, N. Martucciello, L. Peters, N. McEvoy and A. Di Bartolomeo, Environmental Effects on the Electrical Characteristics of Back-Gated WSe2 Field-Effect Transistors, *Nanomaterials*, 2018, **8**(11), 901, DOI: 10.3390/nano8110901.

32 W. Ahmed, L. Yang, U. Zahoor and F. Wang, Oxidation and Defects in WS2 and WSe2: The First-Principle Analysis of Their Monolayer and Bulk Structures, *J. Phys. Chem. Solids*, 2025, **204**, 112775, DOI: 10.1016/j.jpcs.2025.112775.

33 A. Di Bartolomeo, F. Urban, A. Pelella, A. Grillo, M. Passacantando, X. Liu and F. Giubileo, Electron Irradiation of Multilayer PdSe2 Field Effect Transistors, *Nanotechnology*, 2020, **31**(37), 375204, DOI: 10.1088/1361-6528/ab9472.

34 K. Intonti, E. Faella, L. Viscardi, A. Kumar, O. Durante, F. Giubileo, M. Passacantando, H. T. Lam, K. Anastasiou, M. F. Craciun, S. Russo and A. Di Bartolomeo, Hysteresis and Photoconductivity of Few-Layer ReSe2 Field Effect Transistors Enhanced by Air Pressure, *Adv. Electron. Mater.*, 2023, **9**(8), 2300066, DOI: 10.1002/aelm.202300066.

35 Z. Wu, Z. Luo, Y. Shen, W. Zhao, W. Wang, H. Nan, X. Guo, L. Sun, X. Wang, Y. You and Z. Ni, Defects as a Factor Limiting Carrier Mobility in WSe_2: A Spectroscopic Investigation, *Nano Res.*, 2016, **9**, 3622–3631, DOI: 10.1007/s12274-016-1232-5.

36 S.-Y. Lee, S.-H. Kim, K. Watanabe, T. Taniguchi and K.-J. Yee, Role of Hexagonal Boron Nitride Configuration in Gate-Induced Hysteresis of WSe2 Field-Effect Transistors, *Curr. Appl. Phys.*, 2024, **65**, 41–46, DOI: 10.1016/j.cap.2024.06.003.

37 Y. Shi, D. Sang, C. Li, S. Ge, C. Yu, Q. Wang and D. Xiao, Recent Progress of Optoelectronic Applications Based on 2D WSe2 Nanomaterials and Heterostructures: A Review, *J. Mater. Chem. C*, 2025, **13**(36), 18555–18574, DOI: 10.1039/D5TC01545F.

38 M. Wang, C.-Y. Wang, C. Wu, Q. Li, C. Pan, C. Wang, S.-J. Liang and F. Miao, S-Type Negative Differential Resistance in Semiconducting Transition-Metal Dichalcogenides, *Adv. Electron. Mater.*, 2019, **5**(9), 1800853, DOI: 10.1002/aelm.201800853.

39 S. Huo, H. Qu, F. Meng, Z. Zhang, Z. Yang, S. Zhang, X. Hu and E. Wu, Negative Differential Resistance with Ultralow Peak-to-Valley Voltage Difference in Td-WTe_2/2H-MoS_2 Heterostructure, *Nano Lett.*, 2024, **24**(38), 11937–11943, DOI: 10.1021/acs.nanolett.4c03263.

40 T. Lee, K.-S. Jung, S. Seo, J. Lee, J. Park, S. Kang, J. Park, J. Kang, H. Ahn, S. Kim, H. W. Lee, D. Lee, K. S. Kim, H. Kim, K. Heo, S. Kim, S.-H. Bae, S. Kang, K. Kang, J. Kim and J.-H. Park, Junctionless Negative-Differential-Resistance Device Using 2D Van-Der-Waals Layered Materials for Ternary Parallel Computing, *Adv. Mater.*, 2024, **36**(24), 2310015, DOI: 10.1002/adma.202310015.

41 J. H. Kim, B. H. Moon and G. H. Han, Anti-Ambipolar Transport and Logic Operation in Two-Dimensional Field-Effect Transistors Using in-Series Integration of GeAs and SnS2, *Appl. Phys. Lett.*, 2024, **124**(12), 123104, DOI: 10.1063/5.0197983.

42 A. K. Paul, M. Kuiri, D. Saha, B. Chakraborty, S. Mahapatra, A. K. Sood and A. Das, Photo-Tunable Transfer Characteristics in MoTe2–MoS2 Vertical Heterostructure, *npj 2D Mater. Appl.*, 2017, **1**(1), 17, DOI: 10.1038/s41699-017-0017-3.

43 S. Chen, J. Jin, W. Wang, S. Wang, X. Du, F. Wang, L. Ma, J. Wang, C. Wang, X. Zhang and Q. Liu, Thermally Tunable Anti-Ambipolar Heterojunction Devices, *Phys. Chem. Chem. Phys.*, 2024, **26**(35), 23438–23446, DOI: 10.1039/D4CP02937B.

44 K. Kobashi, R. Hayakawa, T. Chikyow and Y. Wakayama, Interface Engineering for Controlling Device Properties of Organic Antiambipolar Transistors, *ACS Appl. Mater. Interfaces*, 2018, **10**(3), 2762–2767, DOI: 10.1021/acsami.7b14652.

45 J. Gusakova, X. Wang, L. L. Shiau, A. Krivosheeva, V. Shaposhnikov, V. Borisenko, V. Gusakov and B. K. Tay, Electronic Properties of Bulk and Monolayer TMDs: Theoretical Study Within DFT Framework (GVJ-2e Method), *Phys. Status Solidi A*, 2017, **214**(12), 1700218, DOI: 10.1002/pssa.201700218.

46 M. Malik, M. A. Iqbal, J. R. Choi and P. V. Pham, 2D Materials for Efficient Photodetection: Overview, Mechanisms, Performance and UV-IR Range Applications, *Front. Chem.*, 2022, 10.

47 V. Chen, H. R. Lee, Ç. Köroğlu, C. J. McClellan, A. Daus and E. Pop, Ambipolar Thickness-Dependent Thermoelectric Measurements of WSe2, *Nano Lett.*, 2023, **23**(10), 4095–4100, DOI: 10.1021/acs.nanolett.2c03468.

